PCCP

ROYAL SOCIETY OF CHEMISTRY

PAPER

View Article Online
View Journal | View Issue

Cite this: *Phys. Chem. Chem. Phys.*, 2025, **27**, 21448

Mass and thermal management strategies for MEA-based CO_2 electrolyzers enabled by physics-based modeling

Huanlei Zhang,†[ab] Jieyang Li †[ab] and Meng Lin *[ab]

Received 8th June 2025,
Accepted 12th September 2025

DOI: 10.1039/d5cp02167g

rsc.li/pccp

Membrane electrode assembly (MEA)-based CO_2 electrolyzers are promising for electrochemical CO_2 reduction (CO_2R) due to their compact design and high current densities. However, performance and durability are often limited by mass transport constraints, thermal gradients, and salt precipitation. We present a comprehensive, non-isothermal, physics-based model that captures multiphase transport of gaseous, liquid, and ionic species, coupled with heat generation, electrochemical reactions, and phase transitions within an MEA-based CO_2 electrolyzer. This model predicts key performance indicators, including CO faradaic efficiency, energy and mass conversion efficiencies, electrode flooding, and salt precipitation. Simulation results identify optimal operating strategies: cathode-side cooling at 10 °C, elevated pressure at 8 atm, and anode-side heating at 80 °C, collectively improving energy efficiency by 42.4% compared to baseline conditions. These findings underscore the importance of precise thermal and mass transport management in advancing scalable CO_2 electrolyzer technologies.

Introduction

Climate change remains one of the most pressing global challenges, driven primarily by increasing atmospheric carbon dioxide (CO_2) emissions from fossil fuel consumption.[1–5] To mitigate these emissions, significant attention has turned toward carbon capture and utilization (CCU) technologies that capture and convert CO_2 into value-added fuels and chemicals.[6–10] Among them, electrochemical CO_2 reduction (CO_2R) in membrane electrode assembly (MEA)-based electrolyzers has emerged as a particularly promising approach.[11–14] These systems offer high energy conversion efficiency owing to their compact, zero-gap architecture, which reduces transport losses compared to conventional flow cells or H-type configurations. Moreover, product selectivity in MEA-based electrolyzers can be finely tuned *via* catalyst engineering.[15–17]

Despite these advantages, the industrial deployment of MEA-based CO_2 electrolyzers faces persistent challenges, particularly at high current densities (>200 mA cm^{-2}). To achieve economically viable operation, systems must maintain high CO_2 utilization and energy efficiency while ensuring long-term stability.[18–20] In particular, long-term stability is highly sensitive to water and ion management. Inadequate control of water transport can lead to electrode flooding, while ionic imbalances often promote the formation of salt precipitates such as K_2CO_3.[14,21–24] Moreover, these mass transport processes are inherently coupled to heat transfer within the device. For example, elevated temperatures increase evaporation rates, enhance ion mobility and electro-osmotic drag, and affect membrane hydration and reaction kinetics. These coupled effects critically impact flooding, salt precipitation, and overall device performance. As a result, local thermal environments can strongly influence flooding behavior, salt formation, and overall device efficiency.[25–27] Therefore, a comprehensive understanding of how heat and mass transport interact is essential for guiding the design and thermal regulation strategies of next-generation MEA-based CO_2 electrolyzers.

Physics-based modeling has been proven effective for revealing complex transport phenomena in MEA-based CO_2 electrolyzers, thereby enabling systematic improvements in their design and operation.[26–28] In recent years, research in this field has made rapid progress; for example, Weng *et al.*[29] and Weber *et al.*[26] established foundational multiphase transport models for gas diffusion electrodes. Subsequently, more studies proposed advanced frameworks that have been fully validated, such as dynamic ion transport and electrolyte composition models,[30] capable of capturing ion depletion and carrier switching effects, as well as comprehensive treatment of multiphase CO_2 reduction kinetics and ion migration.[31] Additionally, recent work has extended to three-dimensional simulations, for example, Liu *et al.*[32] established a 3D model of zero-gap CO_2 electrolyzers and

[a] *Department of Mechanical and Energy Engineering, Southern University of Science and Technology, Shenzhen 518055, China. E-mail: linm@sustech.edu.cn*
[b] *SUSTech Energy Institute for Carbon Neutrality, Southern University of Science and Technology, Shenzhen 518055, China*
† These authors contributed equally to this work.

validated it experimentally under acidic conditions, revealing the impact of flow field design on performance; another study by Abdullah Bafaqeer *et al.*[33] developed a glucose precursor carbon/TiO_2 heterojunction for analyzing electrochemical CO_2 reduction in zero-gap electrolyzers, emphasizing the role of local concentration gradients. These models have significantly improved prediction accuracy under actual operating conditions. However, previous studies mostly used simplified assumptions, such as isothermal conditions, ignoring key thermal gradients and their impact on electrolyzer behavior. Although the latest work by Hurkmans *et al.*[34] incorporated non-isothermal effects, their method mainly assumes similar temperature conditions in the anode and cathode chambers, ignoring potential large temperature variations between electrodes *via* active thermal management. In fact, studies simultaneously capturing multiphase species transport, electrochemical and homogeneous ion reactions, and spatially resolved thermal gradient coupling effects remain limited. In particular, the impact of different temperature environments in the anode and cathode on device performance, stability, and degradation mechanisms is poorly understood. This key gap limits the utility of existing models in guiding the design and operation of robust, scalable CO_2 electrolyzers. Therefore, this article introduces a non-isothermal, multi-physical field coupled framework that explicitly correlates thermal management with electrochemical performance and salt precipitation inhibition, thereby supplementing the above work.

In this work, we develop a comprehensive, non-isothermal, physics-based model for MEA-based CO_2 electrolyzers that explicitly accounts for disparate thermal environments at the anode and cathode. The model captures the coupled transport of gaseous, liquid, and ionic species, incorporates heat generation and dissipation mechanisms, and includes both electrochemical and homogeneous reactions. By enabling the prediction of flooding behavior, salt precipitation, and energy and mass conversion efficiencies under varying temperature boundary conditions, this framework offers new insights into the interplay between mass and thermal management. The validity of the model is substantiated by asymmetric thermal configuration experiments recently reported by our group.[25] The polarization curves and CO faradaic efficiency (FE_{CO}) measured under elevated pressure and asymmetric temperature conditions (Fig. 2d–e) exhibit strong agreement with the predicted trends, while salt precipitation phenomena revealed by EDS mapping and CT imaging (Fig. 3a, d and SI Fig. S12–S15) are consistent with the simulated onset and spatial distribution of K_2CO_3 deposition. The results guide optimal design and operation strategies for improving the performance and durability of MEA-based CO_2 electrolyzers under practical conditions.

Results and discussion

Fig. 1 presents the schematic of the modeling domains and involved physics in this study for a typical exchange MEA-based CO_2 electrolyzer. The key components of the electrolyzer include

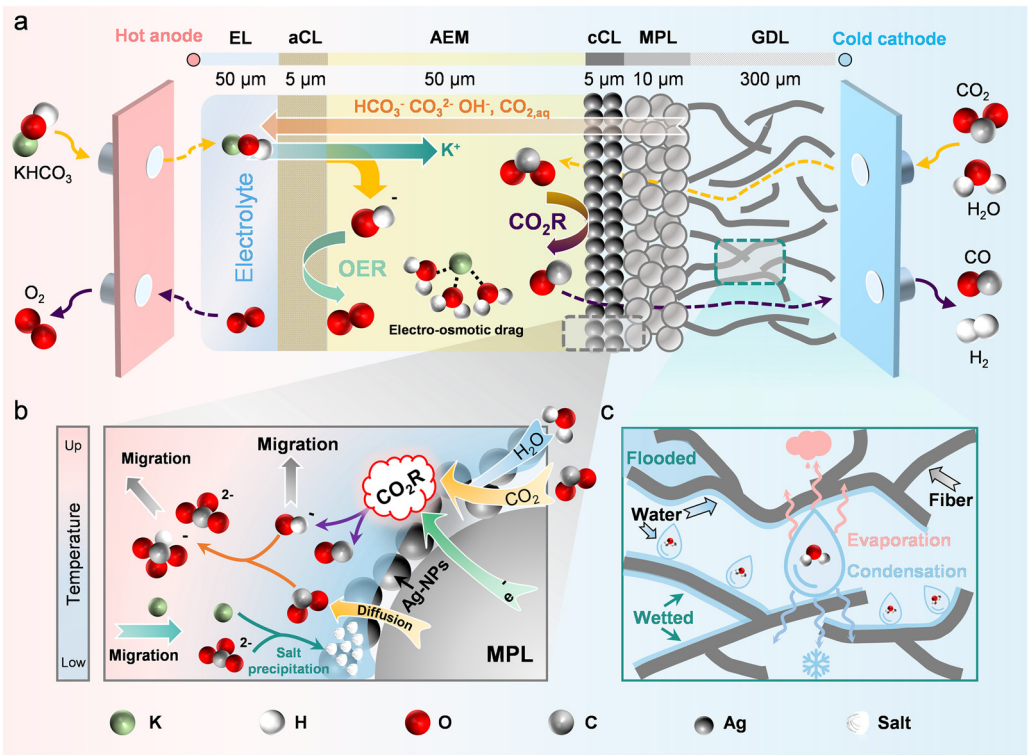

Fig. 1 (a) Schematic illustration of the computational domain for the MEA-based CO_2 electrolyzer model. The model includes the cathode gas flow channel, gas diffusion layer (GDL), catalyst layer (CL), membrane, anode catalyst layer, anode GDL, and anode gas flow channel with all dimensions labeled. Two zoomed-in insets highlight key transport processes: (b) species transport in the catalyst layer, where gaseous CO_2, dissolved ions, and water participate in electrochemical and homogeneous reactions, and (c) water transport in the cathode GDL, which includes vapor–liquid phase change and capillary-driven liquid transport.

a 50 μm electrolyte layer (EL), a 5 μm anode catalyst layer (aCL), a 50 μm anion exchange membrane (AEM), a 5 μm cathode catalyst layer (cCL), a 10 μm microporous layer (MPL), and a 300 μm gas diffusion layer (GDL). 0.1 M $KHCO_3$ was considered as the anolyte and gaseous CO_2 with and without humidification was the feeding reactant at the cathode. A concentration of 0.1 M was selected as the representative benchmark consistent with commonly reported experimental studies. In addition, the anode electrolyte boundary condition is assumed to remain fresh, representing a large reservoir or continuous-feed condition, consistent with conventions in prior CO_2R modeling studies. In our study, we focus on heat and mass transfer within the electrolyzer and their effects on the performance.

In terms of mass transfer, the study covers the following transport phenomena:

(i) aqueous species transport (*i.e.*, CO_2(aq), OH^-, H^+, CO_3^{2-}, HCO_3^-, and K^+) within the EL, aCL, AEM, and cCL. The transport processes including diffusion and migration (eliminated for neutral species, *i.e.*, CO_2(aq)) were solved with Nernst–Planck equation (Fig. 1b, gray arrow). Mass sources induced by electrochemical reactions in the aCL and cCL (Fig. 1b, purple arrow), ionic homogeneous reactions (Fig. 1b, green arrow), and the dissolution of CO_2 into the solution (Fig. 1b, yellow arrow) were accounted for.

(ii) Gaseous species transport (*i.e.*, CO_2(g), CO, H_2, and H_2O) within the cCL, MPL, and GDL (Fig. 1a, yellow dashed arrow). Gas transport includes concentration difference-induced diffusion and pressure difference-induced convection which were described with a convection–diffusion model. Mass sources, including electrochemical reactions in the cCL, CO_2 dissolution, and phase change of water, were accounted for.

(iii) Liquid water and membrane water transport, which mainly occur in the cCL, MPL, GDL, and AEM (Fig. 1c, light cyan arrow). We assumed the relevant liquid water flow only

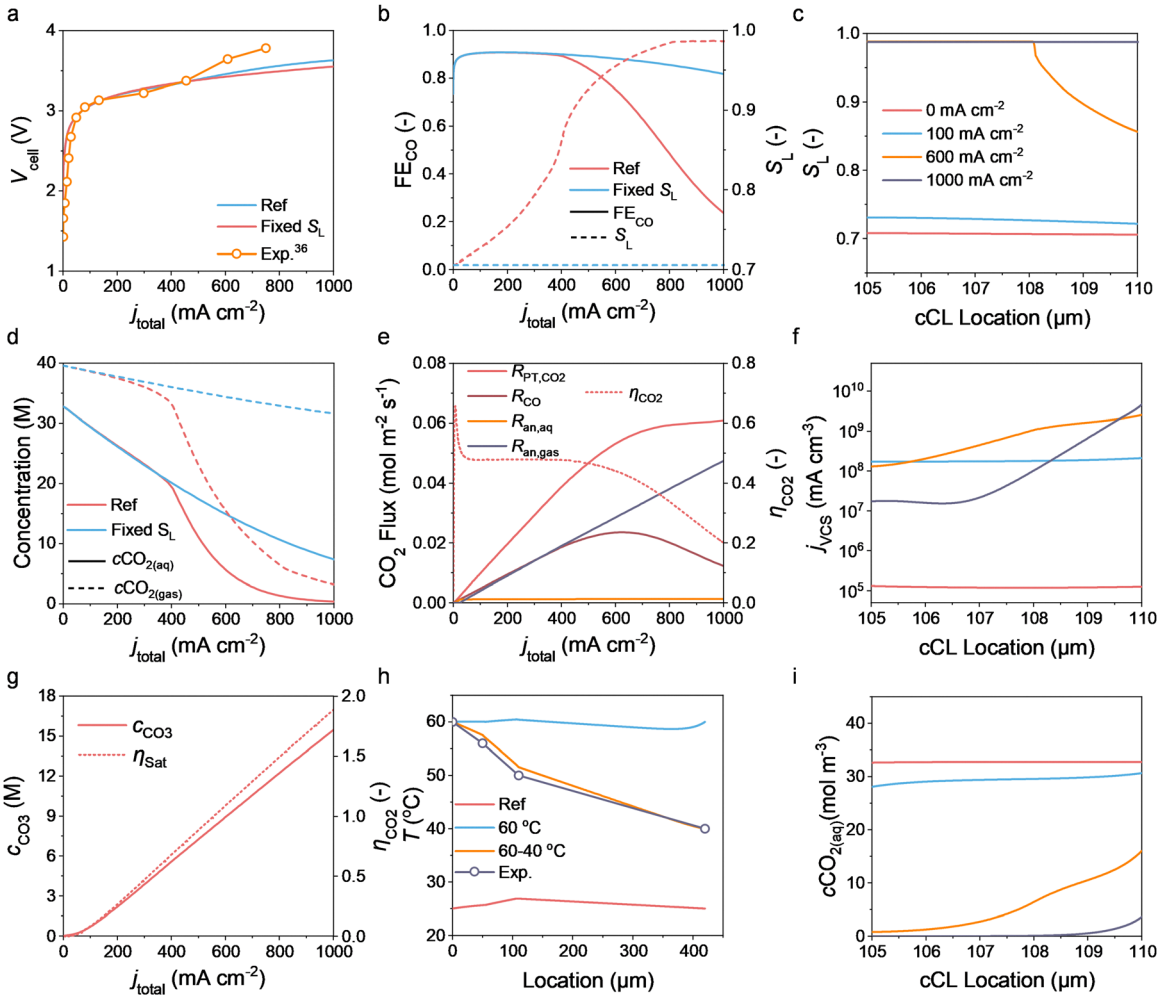

Fig. 2 (a) Calculated and experimental polarization curves for the reference case at 25 °C. (b) Simulated FE_{CO} (left *y*-axis) and S_L (right *y*-axis) as a function of j_{total} for the baseline case. (c) Distribution of S_L within the cCL for different current densities. (d) Average gas-phase CO_2 concentration (CO_2(g)) and dissolved CO_2 concentration (CO_2(aq)) in the cCL as a function of j_{total}. (e) CO_2 flux and η_{CO_2} as a function of j_{total}. R_{PT,CO_2}, R_{CO}, $R_{an,aq}$, and $R_{an,gas}$ represent the breakdown of carbon balance. (f) Volume current density of CO (j_{VCS}) within the cCL for different j_{total}. (g) Averaged concentration of CO_3^{2-} within the cCL, c_{CO3}, and η_{sat} as a function of j_{total}. (h) Temperature profiles over the whole electrolyzer under various temperature conditions. Note that the reference case was at 25 °C. (i) CO_2(aq) concentration profiles within the cCL for different current densities.

happens in the cCL, MPL, and GDL solved with the Darcy's law. Meanwhile, the water transport in the membrane, *i.e.*, AEM in this study, includes diffusion and electro-osmosis dragging. Mass sources for liquid water in the cCL, MPL, and GDL were majorly induced by phase changes, *i.e.*, evaporation and condensation. No mass source was considered within the membrane.

Heat transfer occurs throughout all domains. Specifically, heat conduction was considered for all domains, with additional convection also involved in the cCL, MPL, and GDL. We considered four heat sources due to charge transfer reactions, bulk ionic reactions, liquid–vapor water phase transfer, and Joule heating. We applied different temperature conditions at the left boundary of the electrolyte domain and the right boundary of the GDL, resulting in varying temperature distributions within the electrolyzer to study the effects of thermal regulation.

To predict the regulation of heat and mass transfer on the performance of the CO_2 electrolyzer, we developed a comprehensive physics-based model. This model incorporates key processes such as electrochemical reactions, homogeneous reactions, phase change processes between liquid water and vapor, two-phase flow, and heat and mass transfer. The detailed model development and parameters used for simulation are shown in Section S1, Numerical simulations. The coupled equations were solved by using the finite element method (FEM) implemented in COMSOL Multiphysics 6.1. We validated our model with literature data[36] (Fig. 2a). The validated model was then used as a tool for the optimization and guiding of mass and thermal management strategies for MEA-based electrolyzers. By investigating various temperature regulations, material properties, and operational conditions, we seek to identify optimal settings that maximize CO_2 reduction efficiency as well as CO_2 conversion efficiency. We used both energy and mass conversion efficiencies to quantify the performance of the electrolyzer. The energy conversion efficiency is defined with an exemplary target production of CO:

$$\eta_{\text{energy}} = \frac{j_{\text{CO}} 1.34\ [\text{V}]}{j_{\text{total}} V_{\text{cell}}} \tag{1}$$

where j_{CO} is the partial current density of CO, j_{total} is the total current density, and V_{cell} is the voltage of the electrolyzer. The value 1.34 V corresponds to the thermodynamic potential difference between the oxygen evolution reaction (OER, 1.23 V) and the CO_2 reduction reaction to CO (COER, −0.11 V).

The mass conversion efficiency (η_{CO_2}) is defined as:

$$\eta_{CO_2} = \frac{R_{\text{CO}}}{R_{\text{PT,CO}_2}} \tag{2}$$

where F is the Faraday constant, R_{CO} is the rate of CO generation at the cCL, $R_{\text{PT,CO}_2}$ is the rate at which gaseous CO_2 dissolves into the liquid phase at the cathode. This definition assumes that the unreacted gaseous CO_2 can be recycled, and thus only the CO_2 released at the anode is considered as a net loss. Once dissolved into the catholyte, CO_2 can undergo three distinct pathways:

(1) It may be electrochemically reduced at the cCL to form CO; (2) It may react with OH^- in the electrolyte to form CO_3^{2-} and HCO_3^-, which subsequently migrate across the membrane into the anolyte, contributing to the carbon flux $R_{\text{an,aq}}$; (3) under low-pH conditions at the anode, these anionic species may convert back to CO_2, which then escapes as gas, with this flux designated as $R_{\text{an,gas}}$.

Therefore, the system's carbon balance can be expressed as:

$$R_{\text{PT,CO}_2} = R_{\text{CO}} + R_{\text{an,aq}} + R_{\text{an,gas}} \tag{3}$$

To further assess and quantify the salt precipitation potential under various conditions, we used the ratio between the maximum local K_2CO_3 concentration and the saturation concentration of K_2CO_3. η_{sat} is defined as:

$$\eta_{\text{sat}} = \frac{c_{\text{Max,K}_2\text{CO}_3}}{c_{\text{Sat,K}_2\text{CO}_3}} \tag{4}$$

where $c_{\text{Max,K}_2\text{CO}_3}$ is the maximum local K_2CO_3 concentration and $c_{\text{Sat,K}_2\text{CO}_3}$ represents the saturation concentration of K_2CO_3 and is positively correlated with temperature; higher temperatures yield larger $c_{\text{Sat,K}_2\text{CO}_3}$ values.[35] The CO_2 gas–liquid mass transfer model employed in this study is based on first-principles formulations such as convection–diffusion, Henry's law dissolution, and Nernst–Planck ion transport. These formulations have been widely adopted and validated in previous MEA CO_2R studies.[26,27,29] To simplify the model and facilitate comparison across conditions, $\eta_{\text{sat}} > 1$ is used here as a criterion for the potential onset of salting-out. This threshold does not imply immediate precipitation or failure but indicates conditions where salting-out may begin. In practice, precipitation is subject to lag and dynamic processes such as nucleation, growth, and migration. Future extensions of this model will incorporate experimental insights to more accurately capture these behaviors.

The simulated and experimental polarization curves for the MEA-based CO_2 electrolyzer are shown in Fig. 2a.[36] Two simulation cases are presented: one assuming a constant liquid saturation (S_L = 0.71, *i.e.*, non-flooding) and the other with S_L dynamically solved based on water transport. As shown in Fig. 2b, dynamic S_L increases with increasing current density (j_{total}), reaching values near 0.99 when $j_{\text{total}} > 823.3$ mA cm^{-2}. This increase is due to the reduced cathode-side gas pressure at high current densities (see Fig. S5). Although the impact on V_{cell} is modest (Fig. 2a), the faradaic efficiency for CO (FE_{CO}) drops significantly in the variable S_L case due to the enhanced hydrogen evolution reaction (HER) under flooded conditions. For example, at 1000 mA cm^{-2}, FE_{CO} falls below 0.2, while the fixed S_L case maintains $FE_{\text{CO}} > 0.8$ across the entire range.

Fig. 2c shows the spatial distribution of S_L within the cathode catalyst layer (cCL). At open circuit (0 mA cm^{-2}), a uniform S_L of 0.71 is observed due to intrinsic wettability. As j_{total} increases, S_L increases, especially near the membrane side, reaching 0.99 at 600 mA cm^{-2}. In contrast, the region near the GDL/channel interface retains lower S_L due to higher local pressure, creating a partially flooded cCL. For example, at 600 mA cm^{-2}, S_L near the GDL remains at 0.86 while the membrane-facing side is nearly saturated. This non-uniform flooding explains the moderate drop in FE_{CO} (*e.g.*, ~0.75 at 600 mA cm^{-2}). At 1000 mA cm^{-2}, the entire

cCL is nearly saturated ($S_L \approx 1$), leading to severe flooding and a sharp decline in FE_{CO}.

The average concentrations of gaseous and dissolved CO_2 in the cCL are shown in Fig. 2d. Under dynamic S_L, the dissolved CO_2 concentration drops sharply when $j_{total} > 400$ mA cm^{-2} due to both CO_2 depletion and increased mass transfer resistance caused by flooding. Fig. 2e provides a breakdown of the carbon balance. The CO_2 dissolution flux (R_{PT,CO_2}) increases with current density, while the CO production rate (R_{CO}) peaks at ~630 mA cm^{-2}. The corresponding CO_2 utilization efficiency (η_{CO_2}) declines beyond this point. Notably, the flux of CO_2 released from the anode ($R_{an,gas}$) increases significantly at high j_{total}, indicating greater carbon loss *via* gas-phase evolution.

Fig. 2f shows the local volumetric CO generation rate (j_{vcs}) across the cCL. In flooded regions (high S_L), j_{vcs} is suppressed due to limited CO_2(aq), as also shown in Fig. 2i. Salt precipitation risk is evaluated in Fig. 2g and h. When the local K_2CO_3 concentration exceeds its saturation limit, precipitation is assumed to occur. The ratio η_{sat} exceeds 1 when $j_{total} > 559$ mA cm^{-2}, reaching a peak K_2CO_3 concentration of 8.3 M, suggesting high potential for salt accumulation under high current operation.

Fig. 2h further illustrates temperature profiles across the electrolyzer at various heating configurations, while Fig. 2i shows CO_2(aq) profiles within the cCL at different j_{total}. The decline in CO_2 availability, particularly in flooded regions, further explains the drop in FE_{CO} and performance degradation.

Fig. 3a illustrates the η_{energy} as a function of current density under various anode and cathode temperature conditions. In this section, the cathode and anode temperatures are considered to be fixed, and a linear temperature profile in the membrane links the cathode and anode without solving for heat transfer. This helps to identify the idealized temperature required for both the cathode and anode.

As depicted in the figure, the η_{energy} reaches its maximum at 20–80 °C, *i.e.*, 20 °C in the cathode and 80 °C in the anode, across the current density range of 0–1000 mA cm^{-2}. This observation can be explained by the fact that the FE_{CO} is highest under the 20–80 °C conditions (see Fig. 3b) due to higher CO_2(aq) as a result of low cathode temperature (very close to the isothermal 20 °C case). Meanwhile, a high anode temperature, *i.e.*, 80 °C, leads to lower overpotential for the OER. Note that, although this condition does not result in the smallest V_{cell} (isothermal 80 °C shows the lowest V_{cell}, green curve, but low FE_{CO}), it does correspond to a relatively low V_{cell} (see Fig. 3c). For example, at 500 mA cm^{-2}, the V_{cell} for the 20–80 °C case is 3.22 V, which is only 0.2 V higher than the isothermal 20 °C case, while the FE_{CO} is 0.87 for the 20–80 °C case, which is higher than the 80 °C case (FE_{CO} = 0.24).

Fig. 3d presents the effects of different anode and cathode temperature combinations on η_{energy} at j_{total} of 600 mA cm^{-2}. A current density of 600 mA cm^{-2} was selected as the representative benchmark consistent with commonly reported experimental studies. The results indicate that higher anode temperatures and lower cathode temperatures can maximize η_{energy}, with the peak value occurring at 10–80 °C (η_{energy}= 0.35). Additionally, varying the anode and cathode temperatures also affects the mass conversion efficiency (η_{CO_2}) within the cCL and η_{sat}, an indicator of salt precipitation. As shown in Fig. 3e, at j_{total} = 600 mA cm^{-2}, the maximum value of η_{CO_2} occurs between 10 and 80 °C (η_{CO_2} = 0.48). This is due to the relatively high j_{CO} under these conditions, allowing more CO_2 to be utilized.

For the assessment of salt precipitation, at j_{total} = 600 mA cm^{-2}, the maximum value of η_{sat} is 1.8 at 10–10 °C case (see Fig. 3f). As the temperature of either the anode or cathode increases, η_{sat} decreases, with the lowest value (0.032) occurring at 80–80 °C. This was due to the fact that higher temperature leads to high salt solubility in the cathode, and hence less potential for salt precipitation for a fixed current. Interestingly, merely increasing the anode temperature can also mitigate salt precipitation at the cathode. This effect is primarily attributed to the higher anode temperature enhancing $R_{an,gas}$ (see Fig. S7), which subsequently lowers the CO_3^{2-} concentration at the cathode, thereby reducing salt precipitation.

In practice, the actual temperature distribution within the electrolyzer is highly dependent on the thermal properties of electrodes and membrane, which deviate from the ideal case in which fixed temperatures are assumed for both the cathode and anode with a linear temperature change in the membrane. The exemplary temperature distributions within the electrolyzer, showing both the idealized case and realistic case, are shown in Fig. S8. The temperature differences between the cathode and anode are much smaller than reservoir temperatures due to cross-membrane conduction.

In this section, we solved the heat transfer equation for the electrolyzer taking into account heat sources induced by charge transfer reactions, bulk buffer reactions, phase transfer and Joule heating (see SI eqn (S40)). Fig. 4a shows the simulated cathode and anode temperature difference (δ_T) as a function of $T_{cathode}$ and T_{anode} (see Section S1, Numerical simulations for detailed heat transfer model). We observed that even with differences in $T_{cathode}$ and T_{anode}, the actual δ_T is within 20 °C. This is also confirmed by our dedicated experiment in which we control the channel temperatures of the cathode and anode sides and measured the temperature of the CL (see S2, Experiment).

Under realistic heat transfer conditions, the maximum η_{energy} is 0.32 as shown in Fig. 4b at 10–10 °C case, and the temperature combinations where η_{energy} exceeds 0.3 are completely different from those in the ideal scenarios. This result arises because when the anode temperature is high, heat transfer causes the cathode temperature not to remain sufficiently low. Fig. 4c shows the effect of different anode and cathode temperature combinations on η_{CO_2} under the actual calculated temperature distributions at a total current density (j_{total}) of 600 mA cm^{-2}. The results indicate that in the region where the cathode temperature is below 40 °C, η_{CO_2} exceeds 0.4, which is similar to the results shown in Fig. 3e. Fig. 4d demonstrates the effect of different temperature combinations between the anode and cathode on the precipitation rate of K_2CO_3 (η_{sat}) at j_{total} = 600 mA cm^{-2}, under actual calculated temperature distributions. The trends observed are essentially similar to those under ideal anode and cathode temperature combinations.

This paper proposes three strategies to increase the temperature difference between the anode and cathode. These

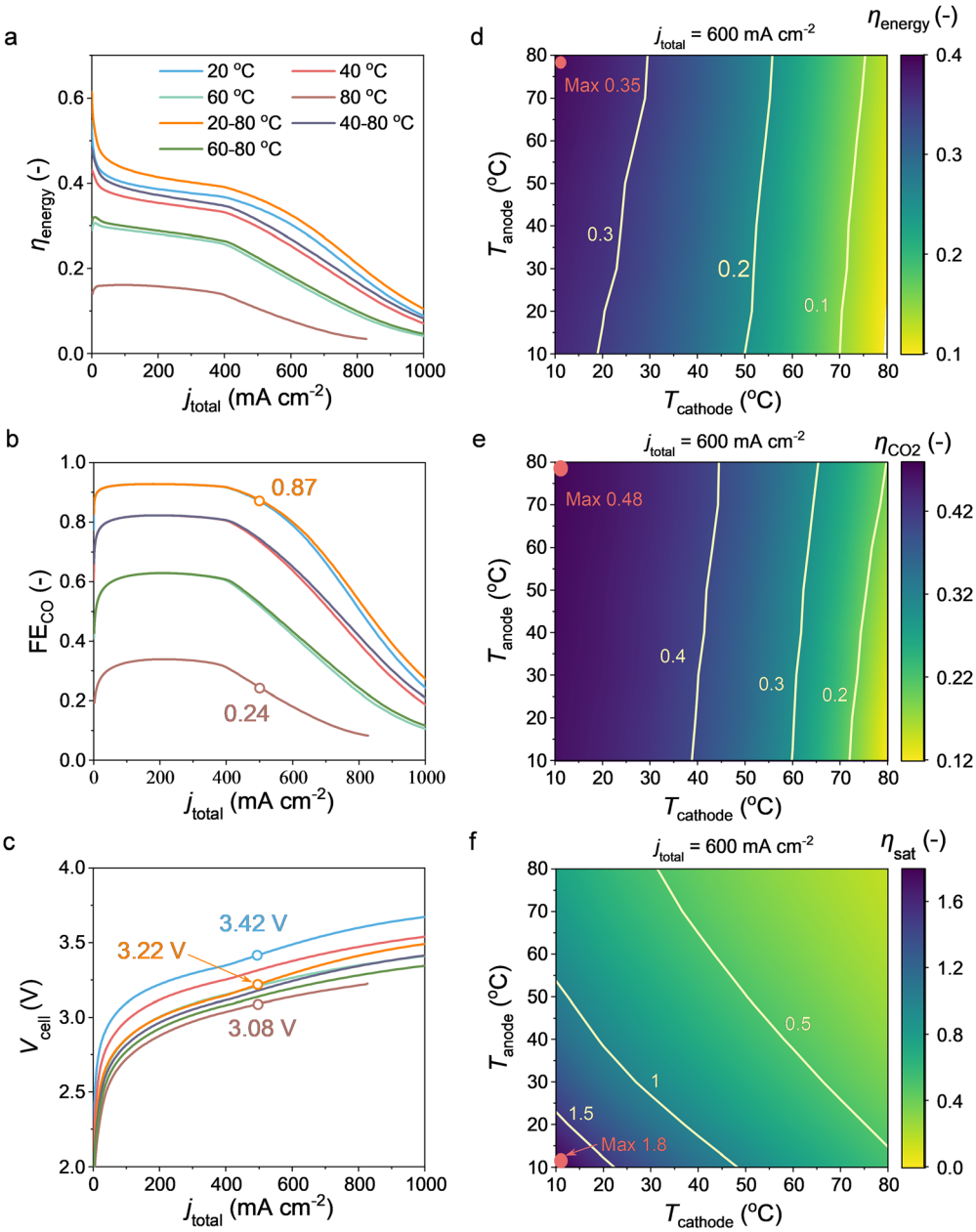

Fig. 3 η_{energy} (a), FE_{CO} (b), and (c) V_{cell} as a function of j_{total} for different temperature cases. (d) Contour maps of η_{energy} (d), η_{CO_2} (e), and η_{sat} (f), as a function of various combinations of T_{anode} and $T_{cathode}$ at 600 mA cm^{-2}.

methods involve adjusting the thermal conductivity of the anion exchange membrane (AEM) denoted as $k_{T,Mem}$, the thermal conductivity of the gas diffusion layer (GDL) denoted as $k_{T,GDL}$, and the thickness of the AEM, denoted as δ_M. Fig. 5a–c display how variations in $k_{T,Mem}$, $k_{T,GDL}$, and δ_M affect the average temperature difference across the catalyst layers (CLs). It is observed that adjusting $k_{T,Mem}$ and $k_{T,GDL}$ can only achieve a limited maximum temperature difference of 35 °C and 50 °C, respectively. Although altering δ_M also effectively modifies the temperature difference, it leads to a decrease in η_{energy} under high current densities (see Fig. 5d) and significantly reduces the CO_2 utilization rate (η_{CO_2}) (see Fig. 5f).

Operating a CO_2 electrolyzer under high pressure is a promising method to enhance CO_2 reduction performance in terms of both η_{energy} and η_{CO_2}, as higher pressures increase CO_2 solubility and availability at the cathode, thereby boosting reaction rates and selectivity. However, this approach can also lead to the precipitation of K_2CO_3 at the cathode due to excessive CO_2 solubility under high-pressure conditions. Increasing the cathode temperature can mitigate this issue by reducing CO_2 solubility. Therefore, this study explores different combinations of cathode temperature and pressure (p_{ref}), while keeping the anode temperature fixed at 80 °C, to optimize CO_2 reduction efficiency and minimize byproduct formation.

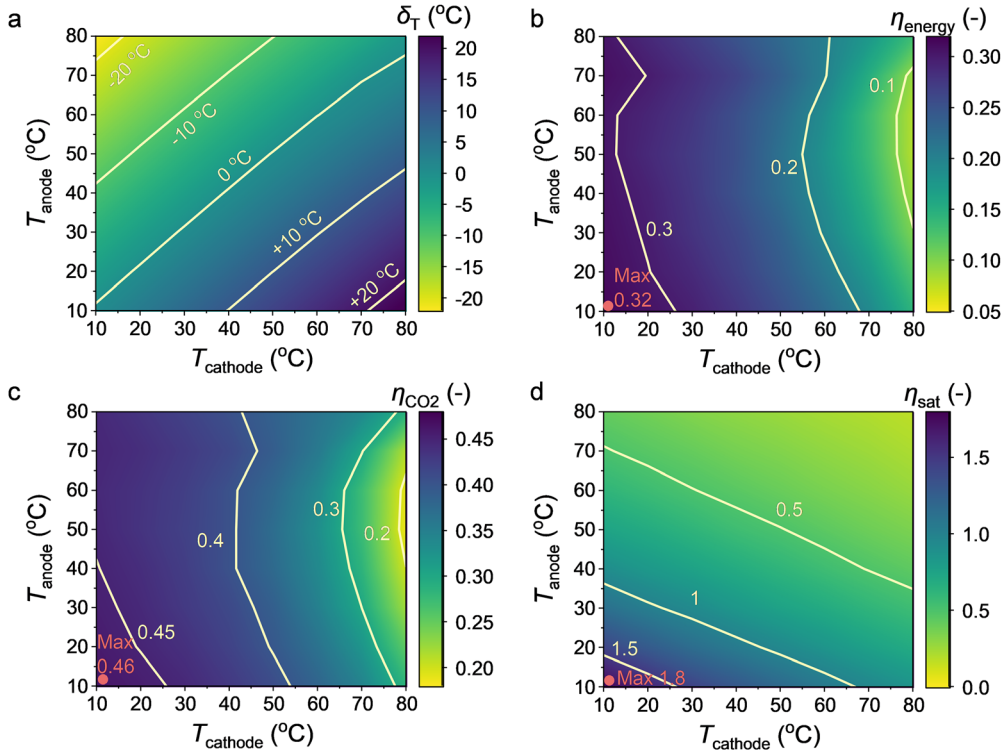

Fig. 4 Simulated temperature differences considering realistic heat transfer for various temperature combinations (a); contour plots of η_{energy} (b), η_{CO_2} (c), and η_{sat} (d) as a function of set T_{anode} and $T_{cathode}$, at 600 mA cm^{-2} under realistic heat transfer conditions.

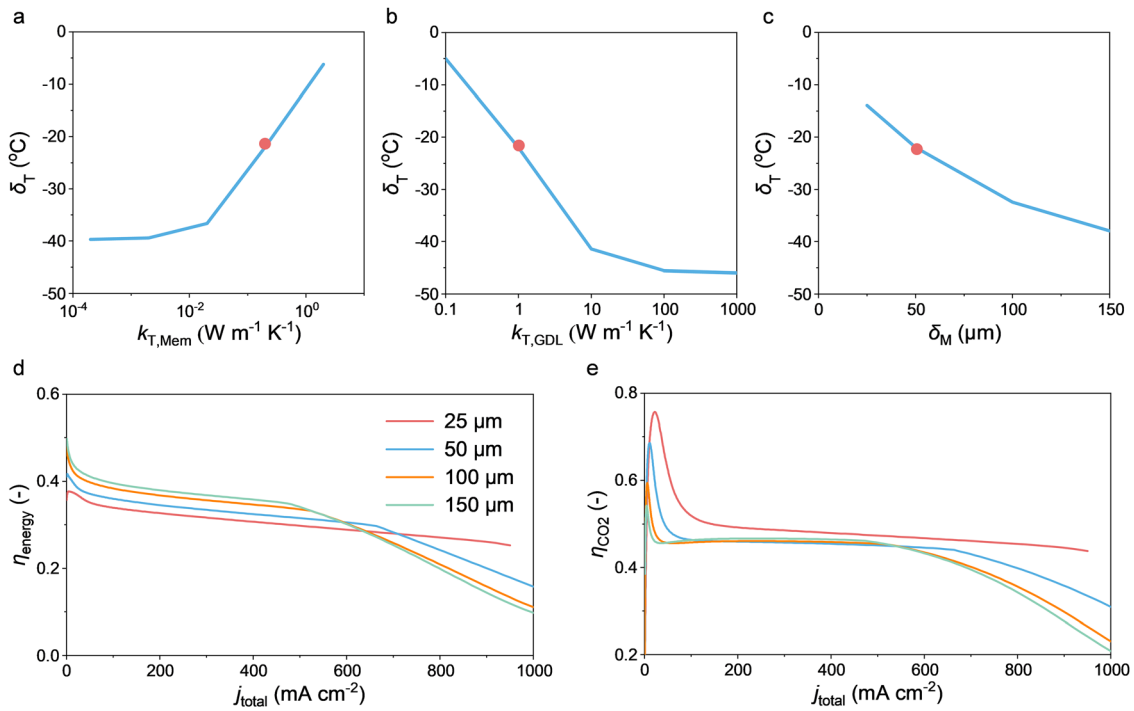

Fig. 5 (a) Impact of varying thermal conductivities ($k_{T,Mem}$) of the AEM (a), thermal conductivities ($k_{T,GDL}$) of the GDL (b) and AEM thicknesses (δ_M) (c) on the average temperature difference between the anode catalyst layer (aCL) and the cathode catalyst layer (cCL). η_{energy} (d) and η_{CO_2} (e) as a function of j_{total} for different AEM thickness cases.

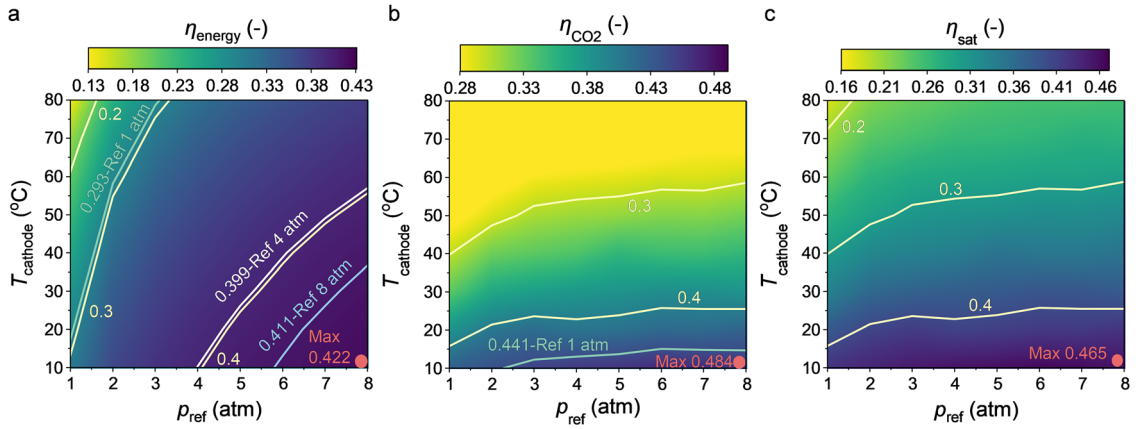

Fig. 6 Contour plots of η_{energy} (a), η_{CO_2} (b), and η_{sat} (c), as a function of various combinations of p_{ref} and $T_{cathode}$ at T_{anode} = 80 °C and j_{total} = 600 mA cm^{-2}.

Under baseline conditions of isothermal 20 °C case, p_{ref} = 1 atm, and j_{total} = 600 mA cm^{-2}, the following results were observed: η_{energy} = 0.316, S_L = 0.86, η_{sat} = 1.16, and η_{CO_2} = 0.508. As shown in Fig. 6a, at j_{total} = 600 mA cm^{-2}, different cathode temperatures and pressures significantly impact η_{energy}. Many combinations of cathode temperature and pressure can achieve $\eta_{energy} > 0.316$. The maximum value of η_{energy}, 0.45, occurs at a cathode temperature of 10 °C and p_{ref} = 8 atm, representing a 42.4% increase compared to the baseline condition. This optimal combination enhances CO_2 reduction efficiency while maintaining low salt precipitation potential. Fig. 6b–d illustrate the effects of different cathode temperatures and pressures on S_L, η_{sat}, and η_{CO_2}, respectively. All combinations show improvement over the baseline scenario. For example, under the optimal conditions of 10 °C cathode temperature and p_{ref} = 8 atm, S_L is maintained at a moderate level, η_{sat} is significantly reduced, and η_{CO_2} is increased. This indicates that by carefully tuning the cathode temperature and pressure, it is possible to achieve high CO_2 reduction efficiency while avoiding issues related to flooding and salt precipitation.

Conclusions

In summary, we developed and experimentally validated a comprehensive non-isothermal, physics-based model for MEA-based CO_2 electrolyzers that, for the first time, accounts for asymmetric temperature profiles between the anode and cathode. Unlike prior models assuming isothermal or uniform conditions, our framework captures coupled heat and mass transport, electrochemical kinetics, and homogeneous ionic reactions under realistic thermal gradients. This enables predictive analysis of key performance metrics, including energy efficiency, CO_2 utilization, flooding, and salt precipitation, under operationally relevant conditions. Simulations reveal that optimal operation at a cathode temperature of 10 °C, an anode temperature of 80 °C, and a pressure of 8 atm yields a peak CO electrical efficiency (η_{energy}) of 0.45 at 600 mA cm^{-2}, representing a 42.4% improvement over baseline conditions. These conditions also mitigate K_2CO_3 precipitation and increase CO_2 utilization (η_{CO_2} = 0.508), underscoring the critical role of temperature and pressure management in enabling efficient and stable operation. By resolving key thermal–mass transport interactions and predicting operational failure modes such as flooding and salt buildup, this study provides new mechanistic insight and actionable design principles for high-performance CO_2 electrolyzers. These results offer a valuable foundation for scale-up and industrial application and present a significant step forward in predictive modeling of electrochemical CO_2 conversion technologies. Future work will explore *in situ* diagnostic techniques, such as tunable diode laser absorption spectroscopy (TDLAS) and fluorescence probes, to directly validate the CO_2 gas–liquid mass transfer behavior predicted by the model. In addition, the framework will be extended in future work to high-load operation and varied electrolyte conditions to further validate the robustness of the proposed strategies.

Conflicts of interest

There are no conflicts to declare.

Data availability

All data related to this paper can be requested from the corresponding author Meng Lin. The supplementary information includes a detailed description of the numerical simulation framework, with schematics of the modeling domains and boundary conditions (Fig. S1), parameters used in simulations (Tables S1–S5), and results of the mesh independence studies (Fig. S4). Additional simulation results are provided, including the relationships between gas pressure, current density, and temperature distributions (Fig. S5–S8). The experimental methods are also described, covering electrode preparation, electrochemical configurations, and CO_2 reduction reaction (CO_2RR) product analysis, supported by a schematic of the experimental system (Fig. S9). Further experimental results are included, such as CO partial current density, Faradaic efficiencies, salt deposition analysis, electrochemical impedance spectroscopy, and stability tests (Fig. S10–S17). See DOI: **https://doi.org/10.1039/d5cp02167g**.

Acknowledgements

The authors acknowledge the National Natural Science Foundation of China (52376191), Guangdong Basic and Applied Basic Research Foundation (2023A1515011595), Guangdong Major Project of Basic and Applied Basic Research (2023B0303000002), and Guangdong grant (2021QN02L562). The Shenzhen Science and Technology Innovation Commission under Grant 20231120185819001 and KCXST20221021111207017, as well as SUSTech High Level of Special Funds under grant no. G03034K001 is also acknowledged for their support. The computation in this work is supported by the Center for Computational Science and Engineering at Southern University of Science and Technology.

References

1 S. J. Davis, N. S. Lewis and M. Shaner, *et al.*, Net-zero emissions energy systems, *Science*, 2018, **360**(6396), eaas9793.
2 C. L. Quéré and J. I. Korsbakken, *et al.*, Drivers of declining CO_2 emissions in 18 developed economies, *Nat. Clim. Change*, 2019, **9**(3), 213–217.
3 W. Rickels, F. Meier and M. Quaas, The historical social cost of fossil and industrial CO_2 emissions, *Nat. Clim. Change*, 2023, **13**(7), 742–747.
4 T. M. Lenton, J. Rockström and O. Gaffney, *et al.*, Climate tipping points—too risky to bet against, *Nature*, 2019, **575**(7784), 592–595.
5 C. Bertram, E. Brutschin and L. Drouet, *et al.*, Feasibility of peak temperature targets in light of institutional constraints, *Nat. Clim. Change*, 2024, **14**(9), 954–960.
6 K. Zhao, C. Jia and Z. Li, *et al.*, Recent advances and future perspectives in carbon capture, transportation, utilization, and storage (CCTUS) technologies: a comprehensive review, *Fuel*, 2023, **351**, 128913.
7 J. Mertens, C. Breyer and K. Arning, *et al.*, Carbon capture and utilization: more than hiding CO_2 for some time, *Joule*, 2023, **7**(3), 442–449.
8 Y. Xie, P. Ou and X. Wang, *et al.*, High carbon utilization in CO_2 reduction to multi-carbon products in acidic media, *Nat. Catal.*, 2022, **5**(6), 564–570.
9 D. C. Carrascal-Hernández, C. D. Grande-Tovar and M. Mendez-Lopez, *et al.*, CO_2 Capture: A Comprehensive Review and Bibliometric Analysis of Scalable Materials and Sustainable Solutions, *Molecules*, 2025, **30**(3), 563.
10 A. E. Geweda, M. E. Zayed and M. Y. Khan, *et al.*, Mitigating CO_2 Emissions: A Review on Emerging Technologies/Strategies for CO_2 Capture, *J. Energy Inst.*, 2024, 101911.
11 C. M. Gabardo, C. P. O' Brien and J. P. Edwards, *et al.*, Continuous carbon dioxide electroreduction to concentrated multi-carbon products using a membrane electrode assembly, *Joule*, 2019, **3**(11), 2777–2791.
12 M. Lan and W. Ren, Electrolytic CO_2 reduction in membrane electrode assembly: challenges in (Bi) carbonate, crossover, and stability, *Next Mater.*, 2025, **6**, 100506.
13 M. Liu, H. Hu and Y. Kong, *et al.*, The role of ionomers in the electrolyte management of zero-gap MEA-based CO_2 electrolysers: A Fumion vs. Nafion comparison, *Appl. Catal., B*, 2023, **335**, 122885.
14 M. Sassenburg, M. Kelly and S. Subramanian, *et al.*, Zero-gap electrochemical CO_2 reduction cells: challenges and operational strategies for prevention of salt precipitation, *ACS Energy Lett.*, 2022, **8**(1), 321–331.
15 W. Yu, Z. Zhang and F. Luo, *et al.*, Tailoring high-performance bipolar membrane for durable pure water electrolysis, *Nat. Commun.*, 2024, **15**(1), 10220.
16 M. Goldman, E. Krall and M. Marufu, *et al.*, Integration of hydrophobic gas diffusion layers for zero-gap electrolyzers to enable highly energy-efficient CO_2 electrolysis to C_2 products, *Chem. Catal.*, 2025, **5**(4), 101235.
17 F. H. Roenning, A. Roy and D. S. Aaron, *et al.*, Mass transport limitations in polymer electrolyte water electrolyzers using spatially-resolved current measurement, *J. Power Sources*, 2022, **542**, 231749.
18 Y. Wang and T. Chu, Improvement of durability of membrane electrode assembly by frame sealing structure in temperature shock, *Front. Energy*, 2024, 1–8.
19 S. Jin, Z. Hao and K. Zhang, *et al.*, Advances and challenges for the electrochemical reduction of CO_2 to CO: from fundamentals to industrialization, *Angew. Chem.*, 2021, **133**(38), 20795–20816.
20 W. Lai, Y. Qiao and J. Zhang, *et al.*, Design strategies for markedly enhancing energy efficiency in the electrocatalytic CO_2 reduction reaction, *Energy Environ. Sci.*, 2022, **15**(9), 3603–3629.
21 S. Rufer, M. P. Nitzsche and S. Garimella, *et al.*, Hierarchically conductive electrodes unlock stable and scalable CO_2 electrolysis, *Nat. Commun.*, 2024, **15**(1), 9429.
22 T. Bi, R. Xue and Y. Jiang, *et al.*, Regulating water transport and salt precipitation for CO_2RR by creating a functional layer, *Int. J. Hydrogen Energy*, 2024, **90**, 784–791.
23 J. Biemolt, J. Singh and G. Prats Vergel, *et al.*, Preventing Salt Formation in Zero-Gap CO_2 Electrolyzers by Quantifying Cation Accumulation, *ACS Energy Lett.*, 2025, **10**, 807–814.
24 J. Disch, L. Bohn and S. Koch, *et al.*, High-resolution neutron imaging of salt precipitation and water transport in zero-gap CO_2 electrolysis, *Nat. Commun.*, 2022, **13**(1), 6099.
25 J. Li, H. Zhang and C. Luo, *et al.*, Non-isothermal CO_2 electrolysis enables simultaneous enhanced electrochemical and anti-precipitation performance, *Nat. Commun.*, 2025, **16**(1), 1–12.
26 L. C. Weng, A. T. Bell and A. Z. Weber, Towards membrane-electrode assembly systems for CO_2 reduction: a modeling study, *Energy Environ. Sci.*, 2019, **12**(6), 1950–1968.
27 L. C. Weng, A. T. Bell and A. Z. Weber, A systematic analysis of Cu-based membrane-electrode assemblies for CO_2 reduction through multiphysics simulation, *Energy Environ. Sci.*, 2020, **13**(10), 3592–3606.
28 J. Park, E. D. Kim and S. Kim, *et al.*, Deriving an Efficient and Stable Microenvironment for a CO_2 MEA Electrolyzer by Reverse Osmosis, *ACS Energy Lett.*, 2024, **9**, 3342–3350.
29 L. C. Weng, A. T. Bell and A. Z. Weber, Modeling gas-diffusion electrodes for CO_2 reduction, *Phys. Chem. Chem. Phys.*, 2018, **20**(25), 16973–16984.
30 V. M. Ehlinger, D. U. Lee and T. Y. Lin, *et al.*, Modeling Planar Electrodes and Zero-Gap Membrane Electrode

Assemblies for CO_2 Electrolysis, *ChemElectroChem*, 2024, **11**(7), e202300566.
31 J. C. Bui, E. W. Lees and D. H. Marin, *et al.*, Multi-scale physics of bipolar membranes in electrochemical processes, *Nat. Chem. Eng.*, 2024, **1**(1), 45–60.
32 R. Wang, S. Yuan and R. Xue, *et al.*, A 3D Numerical Study on Flow Field Designs in Zero-Gap CO_2 Electrolyzers, *Energy Fuels*, 2025, **39**(8), 3942–3953.
33 A. V. Dighe, P. K. R. Podupu and V. V. Gande, *et al.*, Group contribution method for rapid estimation of crystal growth rates, *Chem. Eng. Res. Des.*, 2024, **203**, 140–148.
34 J. W. Hurkmans, H. M. Pelzer and T. Burdyny, *et al.*, Heating dictates the scalability of CO_2 electrolyzer types, *EES Catal.*, 2025, **3**(2), 305–317.
35 R. C. Moore, R. E. Mesmer and J. M. Simonson, Solubility of potassium carbonate in water between 384 and 529 K measured using the synthetic method, *J. Chem. Eng. Data*, 1997, **42**(6), 1078–1081.
36 O. S. Romiluyi, Design and Investigation of Membrane-Electrode Assemblies for the Electrochemical Reduction of CO_2, PhD thesis, University of California, Berkeley, 2022.